FAST X-RAY IMAGING OF A FLUIDIZED BED: IMPACTS OF SUPERFICIAL VELOCITY AND BED INTERNALS

Amir Farzad Forughi, Andrew Mezo, Alexandra Rigby and Christian Veenstra

Coanda, A Tetra Tech Company
Burnaby, BC Canada

18 November 2021

Abstract

In many industrial applications, non-intrusive measurements of visually opaque processes are key to understanding, optimization, and future development. X-ray imaging systems are commonly used to probe such applications, providing, with the correct interpretation, a snapshot of the density distribution. For dynamic multiphase processes such as fluidized beds, solids-laden gas jets, industrial tailings processing, and cavitation, it is imperative that this snapshot image is taken on a very short timescale, in order to capture the required intricacies and details. In this article, we demonstrate the capabilities of our fast (50 ns pulse length) X-ray system, by testing it on different gas-solid fluidized beds consisting of sand and fluid catalytic cracking (FCC) solids at various fluidization velocities. Using this X-ray system, we demonstrate the impact of various internals including sheds (chevron baffles) and intrusive probes on the gas holdup. The sheds were observed to considerably disrupt the emulsion phase, while circular tubes (i.e. probes) had little effect, matching their desired functionalities. These results show that X-ray imaging is an essential tool for providing insights and furthering the research and development of challenging industrial applications.

I. Introduction

Fluidized beds are well-established technologies that are widely used in process engineering. Their high contact area for reactions, efficient mixing, and superior heat and mass transfer characteristics make them ubiquitous in various industrial applications such as gasification, granulation, drying, combustion, etc. Despite having been well-established and studied over the past several decades, there remains a large demand for accurate and affordable measurement techniques to research the hydrodynamics of fluidized beds [1].

Numerous intrusive and nonintrusive measurement techniques have been used to study fluidized beds. Intrusive methods are generally less expensive and are easier to build and maintain [1]. Although nonintrusive optical techniques have been employed in a few studies [2], the majority of optical sensors are classified as intrusive because they must be in direct contact with the solids [3]–[6], often resulting in unavoidable flow disruptions. Recently, an extensive effort has been made towards understanding these effects in order to minimize the induced disturbance [7]–[11]. Optical techniques are usually effective when detecting voids or tracking species is the main goal. However, quantitative measurement of the local density is often inaccurate without precise calibration, which can be particularly difficult because of the differences in the optical properties of particles consisting of different materials and size distributions [12].

Nonintrusive methods include a number of techniques such as electrical capacitance tomography [13]–[16], radioactive tracer measurement [17], and radiation attenuation methods that are employed to measure the density of the emulsion phase inside the bed. X-ray imaging has been used since the 1950s to study fluidized beds, and this has proven to be an effective and reliable tool for investigating these multiphase systems [18]–[21]. There are a wide variety of X-ray densitometers available commercially, including basic methods for average density measurement in which no local information can be obtained, or more sophisticated tomographic techniques that provide local density profiles within the measurement volume [1], [2], [22]–[30]. Although these techniques are relatively costly due to the equipment expenses and operational costs [2], [31], they provide detailed insight into various features of the flow hydrodynamics and are effective tools for fluidized bed density investigations, which can provide the results necessary for validation of available theories and numerical models [27], [32]–[35].

In this article, a digital X-ray system for the measurement of two-phase systems is presented. The measurement system was developed for the measurement of industrial multiphase systems including fluidized beds. To evaluate the utility of the imaging system, X-ray measurements of a 13 cm diameter fluidized-bed filled with different particles and under different fluidization conditions were performed. The resulting images were processed to generate voidage or density distribution maps. Using this X-ray system, the effects of different internal objects including a shed (chevron baffle) and cylinder on the hydrodynamics of the bed were investigated. The experimental results demonstrate the significant industrial and scientific value of X-ray imaging.

II. Methodology

1. Fluidized Bed Column

An acrylic fluidization column with a 13 cm diameter and a height of 112 cm was designed and constructed for fundamental fluidized bed research; see illustration in Figure 1 for an overview of this apparatus. The particles within the column are fluidized using gas injected through a windbox that is separated from the particles by a stainless steel mesh. The mesh size is selected based on the size distribution of the particles such that the particles are blocked from entering the wind-box during or after an experiment. Multiple ports are available on the column at different heights and angular positions to facilitate the connection of the instrumentation for a given experiment.

To study the effect of sheds, an 8 mm thick shed with 38 mm long wings which spanned the entire column diameter was used. Sheds are frequently used in scrubbers and strippers to disrupt the flow and facilitate mixing. Additionally, to investigate the effect of cylindrical intrusive probes on the dynamics of the bed, an 18 mm diameter cylinder was inserted into the column both to the center and the entire diameter of the column. Such probes are generally assumed to have a minimal effect on the bed hydrodynamics. No additional probe or instrumentation is connected to the column in order to facilitate complete visualization of the flow dynamics by the X-ray imaging system.

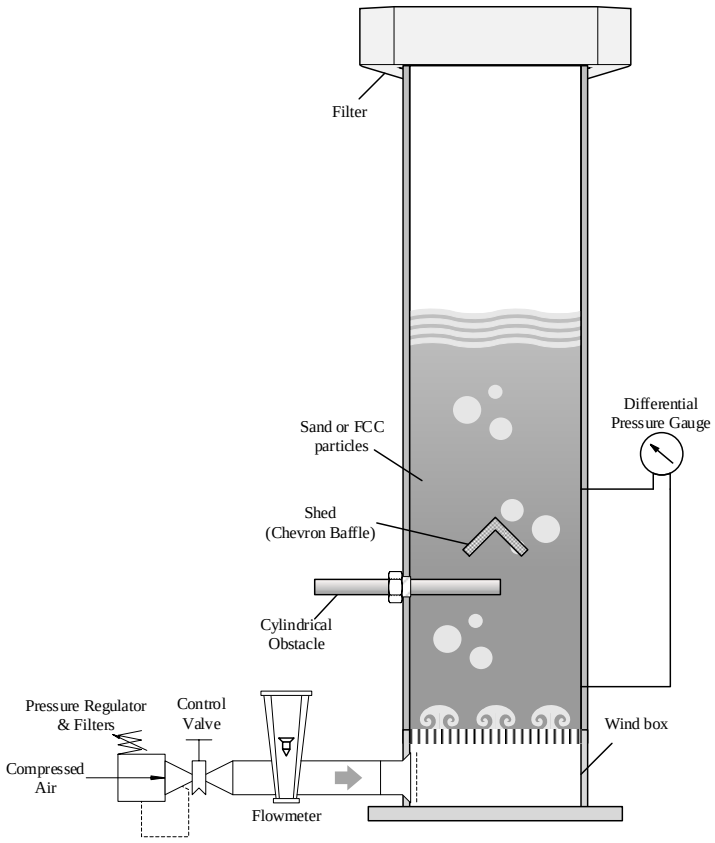

Figure 1 Schematic of the fluidized bed column. The drawing is not to scale.

2. X-ray System

A pulsed X-ray imaging system was mounted onto a multi-axis traverse (see Appendix A for more details). The X-ray source and detector panel can move independently in two directions (vertical and horizontal) and the entire assembly can spin around the centre axis, providing effectively four degrees of freedom for the imaging system. This design allows significant freedom for choosing the optimal source-object-detector configuration in a given experiment. The imaging system, illustrated in Figure 2, is housed in a lead bunker and is designed to contain X-ray radiation within the standards of the Canadian Nuclear Safety Commission (CNSC). The bunker is raised to an elevation of 3.3 m and has an additional 5.5 m of headspace, which facilitates the testing of large experimental apparatus including fluidized beds. In these experiments, the horizontal source-detector distance was 1.2 m, and the horizontal source-object distance is 0.71 m.

The X-ray source is a Golden Engineering® XR200, delivering 50 ns pulses in a cone-beam geometry with a fixed 150 kVp X-ray tube potential (see Appendix B for more details). The source can generate up to 10 pulses per second and can be triggered externally. The detector is a 16-bit, flat-panel Konica Minolta® VisionDR iRay™ 1417CK with a Cesium-Iodide scintillator and provides a 34.3 cm by 41.9 cm imaging area comprised of 2304 by 2800 pixels, equivalent to 150 µm pixel spacing.

This short X-ray pulse length is beneficial when measuring transient events, preventing artifacts including motion blur produced by the fast movement of objects in the images. To traverse a 150 µm pixel within the 50 ns pulse requires speeds over 3000 m/s adjacent to the detector, equivalent to Mach 8.7 in air at ambient conditions. Consequently, the X-ray system is capable of capturing sharp and clear images of fast processes with no motion blur, even at hypersonic air velocities.

To capture longer exposure times and generate time-averaged results, two approaches can be considered. The time-averaged results can be obtained by averaging several single-pulse images, or multiple exposures on the same detector image can be used to create a time-averaged image. Due to the low recording speed of the detector, it is significantly quicker to take a multi-pulse image with the same overall detector exposure. However, as the intensity is a non-linear (Lambertian) function of the density, multi-pulse images cannot be converted to the true average density. In many cases, the typical difference between the true average density and that calculated from the multi-pulse image agree to within a few percent.

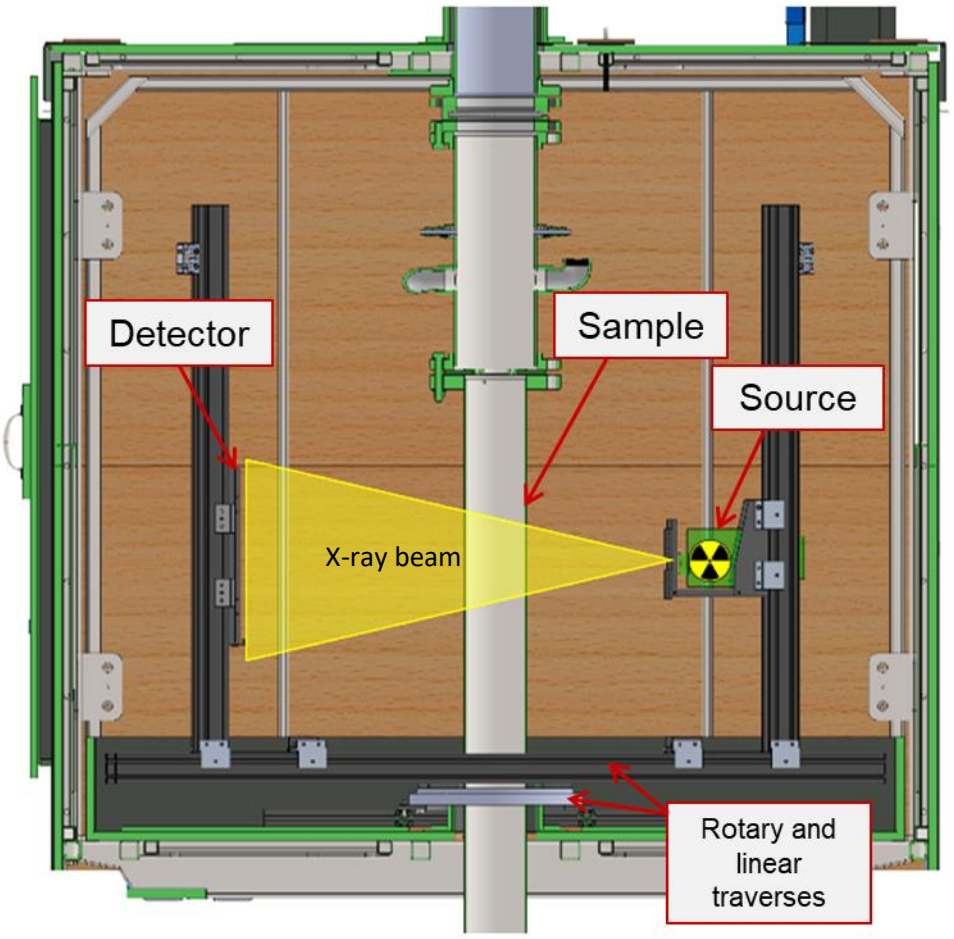

Figure 2 Schematic of the X-ray bunker and imaging system. The bunker is roughly 2.5 m by 2.5 m by 2.5 m. For the current set of experiments, the source-sample distance is set to be 0.71 m and the source-detector distance is 1.4 m.

3. Calibration Procedure

Each X-ray image recorded by the detector measures the intensity of the radiation that was transmitted through the sample in Figure 2. To convert these X-ray images from intensity into units of density, we use the following calibration procedure.

Disregarding secondary scattering, the measured intensity from monochromatic radiation is attenuated according to Beer's Law:

$$\mathrm{I} = \mathrm{I}_0 \mathrm{e}^{-\mu_\mathrm{m} \rho \, x} + \mathrm{I}_\mathrm{B} \,, \tag{1}$$

where I_B is the intensity of the background radiation, I_0 is the intensity of the emitted radiation from the source with no attenuation, and μ_m, ρ, and x are the mass attenuation coefficient, density, and thickness of the material within the test section, respectively. By comparing two images, with and without the sample material, the X-ray image can be readily converted from intensity to a product of the material's properties, μ_m and ρ, and thickness x.

To isolate the thickness of solid material, x, through which the detected X-ray was transmitted, a calibration device, comprised of different thicknesses of acrylic was used. This calibration device is included in every test image containing the real material and can be used to convert the entire image into acrylic

thickness, x_a, by comparing the values of $\mu_m \rho x$ with the known thickness values of the calibration device. For sample materials made from low atomic number elements, Z, the attenuation coefficient of acrylic and the material are similar and so the true material thickness is approximately equal to $x_a \rho_a / \rho$, where ρ_a is the acrylic density. In higher Z cases, the material's attenuation coefficient, μ_m, is very different from that of acrylic and an additional image to convert from x_a to x is required. This can be accomplished by, for instance, imaging a ramp containing the material alongside the acrylic calibration device. Additionally, we observe that our X-ray system is not monochromatic and so beam hardening can contribute to measurement uncertainty.

Having converted the detected intensity image into the amount of sample material passed through by the X-ray beam, the data can be further transformed into maps of bulk density, ρ_{bulk}, or voidage, $\varepsilon = 1 - \rho_{bulk}/\rho_{particle}$, to describe the average behaviour within the test section. It is important to recollect that the recorded image is formed from the interaction of the X-ray with the material along the X-ray's path, and therefore the produced density map does not represent a slice of the test section, but rather the average density of the material passed through by the X-ray beam. This can make interpretation more difficult, especially given that the X-rays are emitted in a cone and so do not pass through the test section as parallel beams. Nevertheless, these images yield valuable information about the observed processes.

III. Results and Discussions

Beds of packed sand or FCC were fluidized using compressed air, and their dynamics probed by taking fast X-ray images which were post-processed to output voidage maps. These images capture the variation in voidage due to air velocity, bed material, and the effect of obstacles such as sheds and intrusive probes. By taking both single-pulse and multi-pulse images, instantaneous snapshots and time-averaged phenomena in the fluidized bed were recorded, thus providing valuable insight into the bed behaviour.

1. Impact of Particle Type and Superficial Velocity

Increasing the velocity of the injected air changes the fluidization regime of the bed (see Table 1 in Appendix C for more details). In these experiments, the investigated air velocity and particle type show packed bed, bubbling fluidization, and slugging fluidization behaviour. By averaging multi-pulse X-ray images, the average voidage of the sand bed at various fluidization velocities was calculated.

As illustrated in Figure 3, the voidage of the fluidized sand at different superficial velocities was measured using the X-ray system. The sand particle sample is a Geldart B group particle and has a minimum fluidization velocity of 0.057 m/s. This minimum fluidization velocity is calculated based on the models available in the literature (Appendix C) and confirmed experimentally by measuring the hold-up pressure in the column. Group B beds exhibit low expansion coefficients and tend to form bubbles at the onset of fluidization [36]. As expected, this series shows the sand transitioning from a packed bed to bubbling, and slugging regimes with increasing fluidization velocity. Higher superficial velocity results in a smoother voidage gradient compared to a step function (slumped bed), to a more uniform distribution at a superficial velocity of 0.45 m/s can be clearly seen in Figure 5a. It must be mentioned that these multi-pulse images are equivalent to 75 single-pulse images and so do not have the temporal resolution to show any individual bubbles.

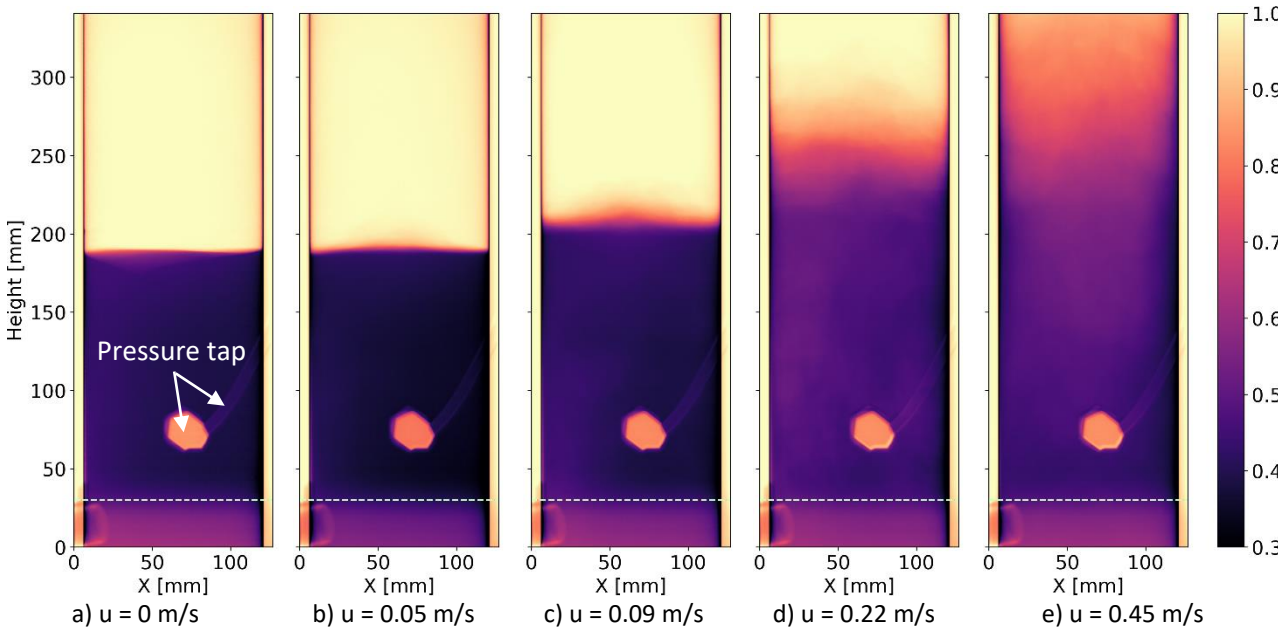

Figure 3 Average voidage of fluidized sand (300 µm) group-B particles at various fluidization velocities. The dashed line shows the approximate position of the grid. The pressure tap connection is outside the column. The colormap shows the voidage value.

In Figure 4, the average voidage of FCC at different fluidization velocities is shown. Similar to Figure 3, these average voidage images were calculated from averaged multi-pulse X-ray images, equivalent to 125 single-pulse images. Unlike sand, FCC is a Geldart group A particle and is expected to fluidize and expand significantly before transitioning into the bubbling fluidization regime. This FCC sample has a minimum fluidization velocity of 0.003 m/s and can be seen to move from a packed bed to the slugging regime when the air velocity is increased from zero to 0.45 m/s.

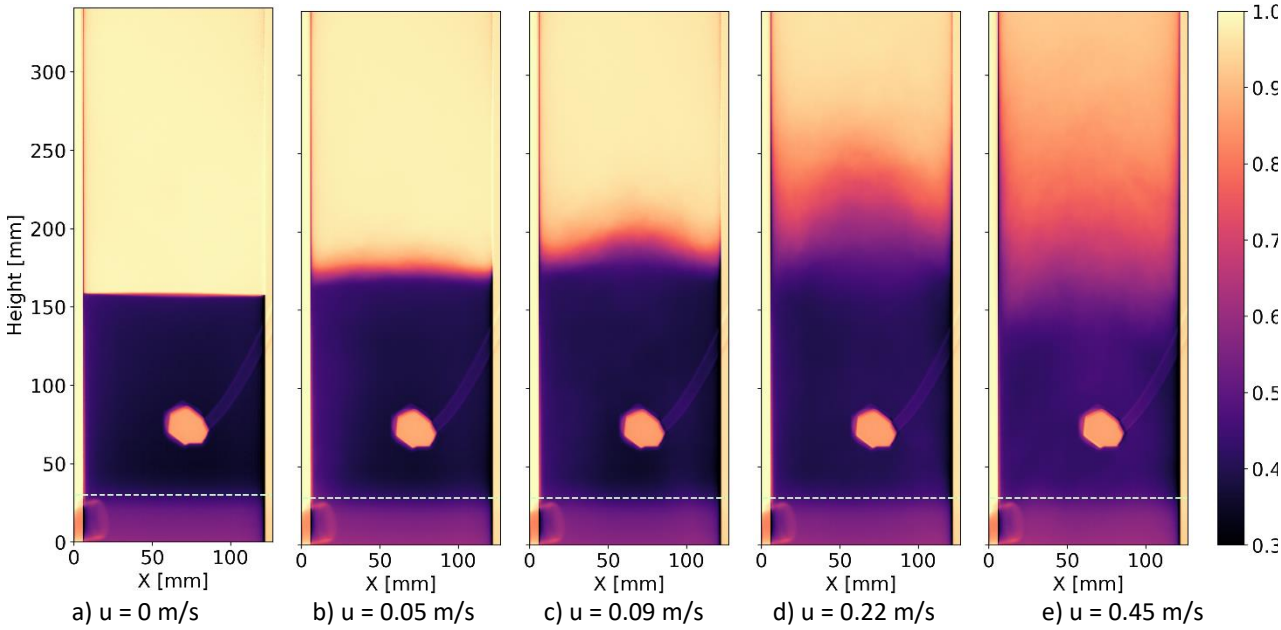

Figure 4 Average voidage of fluidized FCC (85 µm) group-A particles at various fluidization velocities. The dashed line shows the approximate position of the grid. The pressure tapconnection is outside the column. The colormap shows the voidage value.

To be able to compare the particle distribution quantitatively, the voidage variation as a function of the height is illustrated in Figure 5. The different behaviour of the sand and FCC particles at identical superficial velocities is evident.

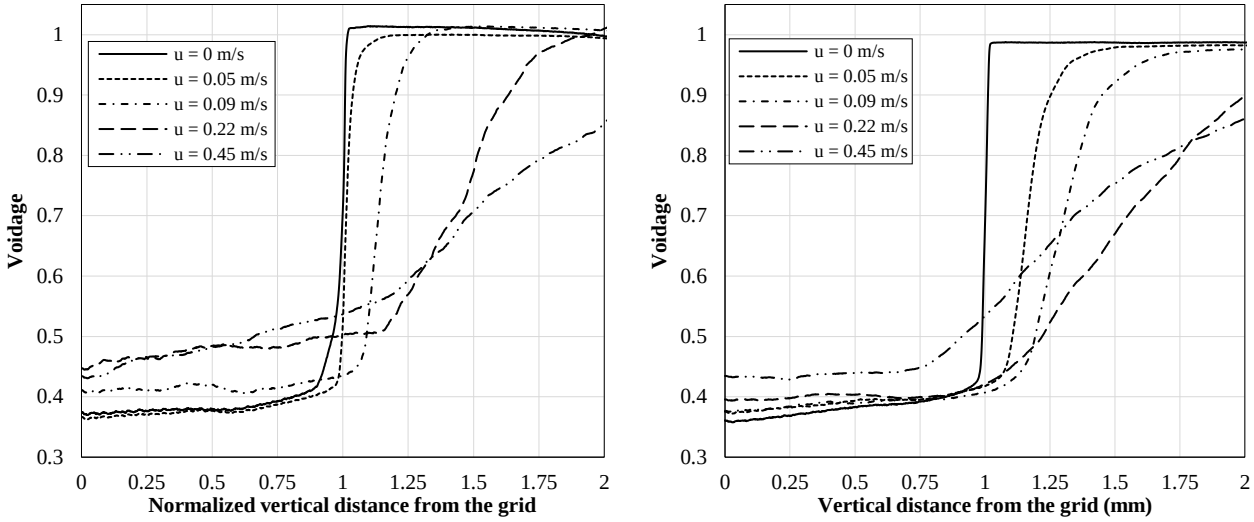

a) Sand b) FCC

Figure 5 The variation of the bed voidage as a function of the height for sand and FCC particles at different superficial velocities. The x-axis shows the height normalized with the packed bed height.

To capture the instantaneous voidage within the fluidized beds, single-pulse X-ray images were taken. In Figure 6a, the voidage from four single-pulse X-ray images is shown next to the averaged voidage in Figure 6b for a superficial velocity of 0.09 m/s for sand. At this velocity, the fluidized bed is expected to be in the bubbling regime. At this velocity, bubbles can often be seen at the free surface of the bed in the single-pulse images, in keeping with the multi-pulse image voidage profile which shows the averaged distribution of the sand over time.

When the fluidization velocity is increased to 0.22 m/s for sand in Figure 7, the single-pulse images show larger bubbles (greater than column's radius) both at the bed surface and within the bed itself, indicative of the emerging of the slugging regime. This chaotic motion and fine structure shown in the single-pulse images is completely smoothed out in the averaged multi-pulse image in Figure 7b. By taking both fast, single-pulse images and averaged, multi-pulse images, a better understanding of the bed dynamics at both short and long time scales is attained.

The large bubbles seen within the bed in Figure 7a for sand can be contrasted against Figure 8a when FCC particles were used with the same fluidization velocity and are in the same slugging fluidization regime. These single-pulse images show dynamic behaviour, where the FCC particles remain mostly in the lower half of the test section but bubbles can raise a significant number of the particles to double the packed bed height. Similarly, the multi-pulse image shown in Figure 8b, illustrates the time-averaged voidage distribution in the bed.

These voidage maps, taken as single-pulse snapshots and as multi-pulse time averages for both sand and FCC at these different air velocities behave as expected for their calculated fluidization regime. The intricate single-pulse images illustrate the unpredictable and chaotic nature of these fluidized beds, while

the averaged images are useful for determining the average bed behaviour. Having conducted these baseline tests, the X-ray imaging system can now be confidently used to evaluate the flow conditions of more challenging experiments, namely when the internals are introduced into the fluidized bed.

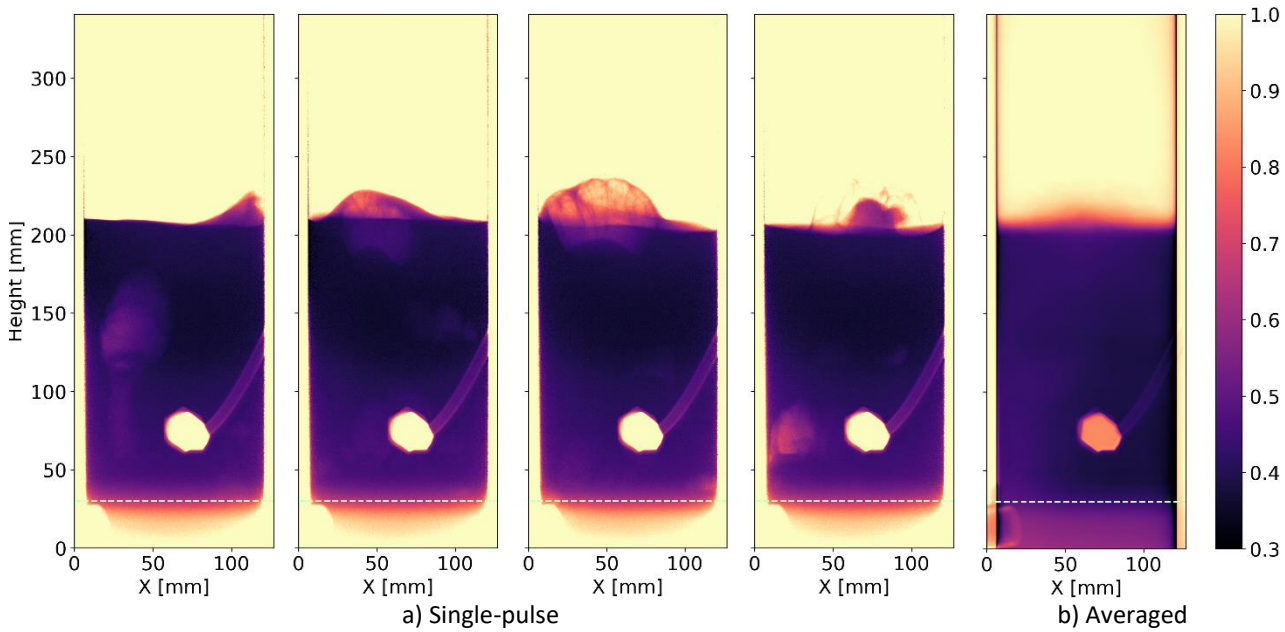

Figure 6 Voidage of fluidized sand (300µm) group-B particles at fluidization velocity u = 0.09 m/s. The averaged image is effectively measured over 75 pulses. The dashed line shows the approximate position of the grid. The pressure tap connection is outside the column. The colormap shows the voidage value.

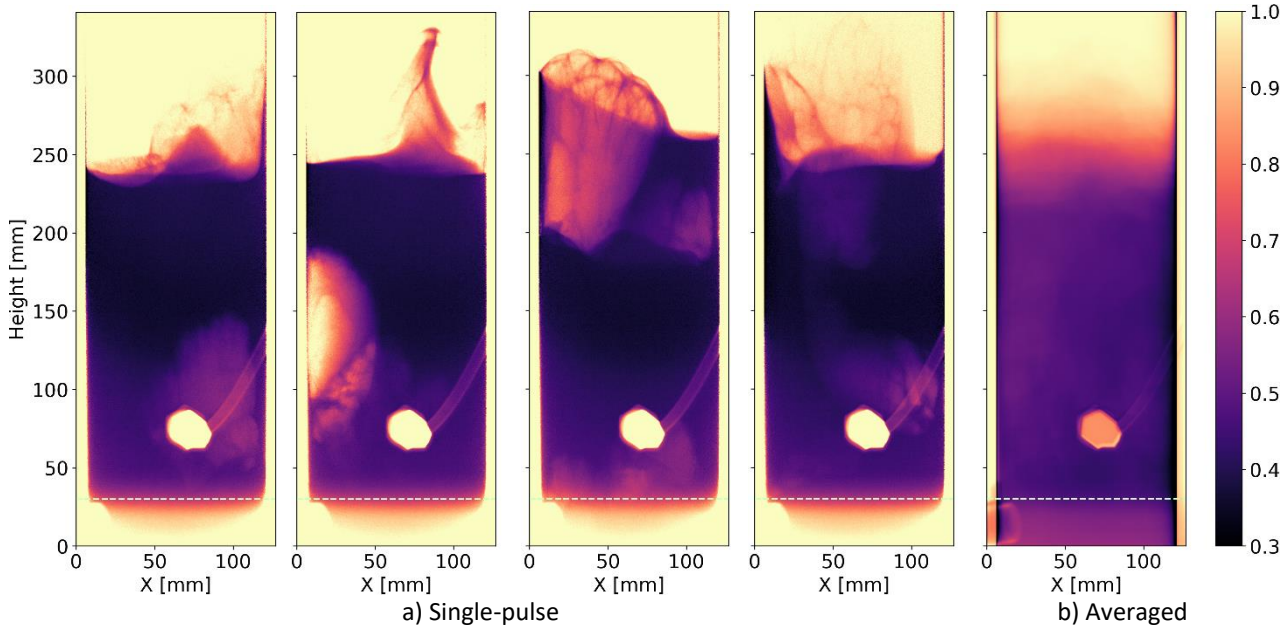

Figure 7 Voidage of fluidized sand (300µm) group-B particles at fluidization velocity u = 0.22 m/s. The averaged image is effectively measured over 75 pulses. The dashed line shows the approximate position of the grid. The pressure tap connection is outside the column. The colormap shows the voidage value.

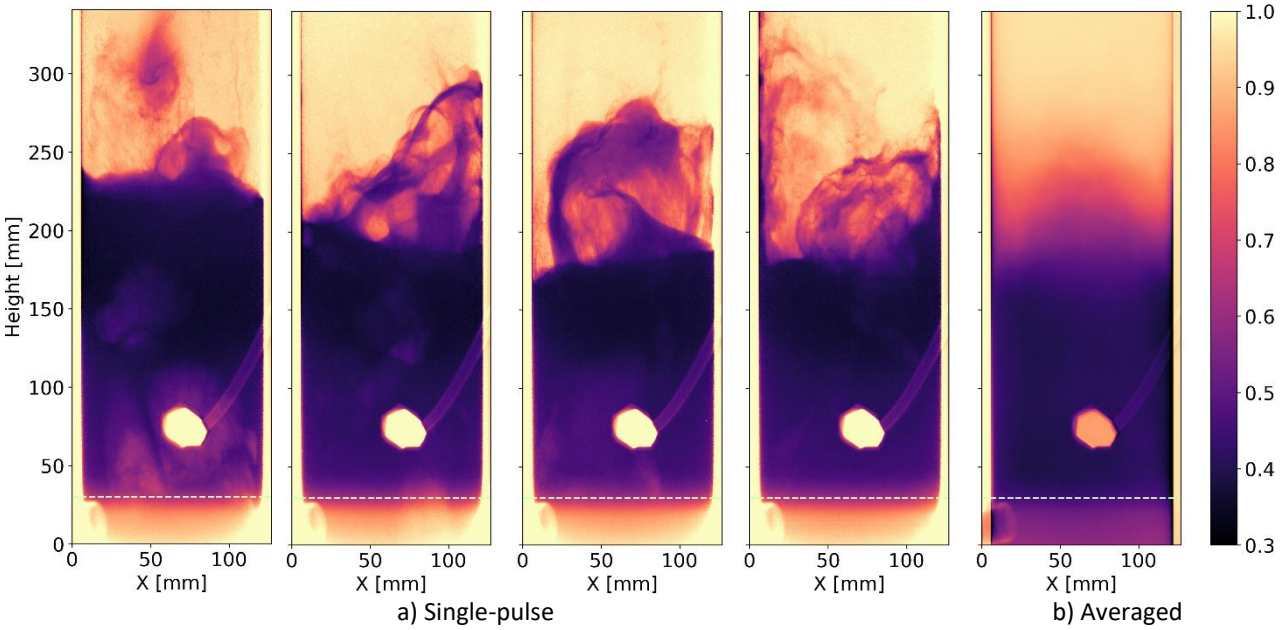

Figure 8 Voidage of fluidized FCC (85 µm) group-A particles at fluidization velocity u = 0.22 m/s. The averaged image is effectively measured over 125 pulses. The dashed line shows the approximate position of the grid. The pressure tap connection is outside the column. The colormap shows the voidage value.

2. Impact of internal obstacles on the bed dynamics

Sheds are commonly used in fluidized beds to disturb the flow and increase mixing [37]. It must be noted that to study the impact of these internals, the slumped bed height was increased to 290 mm. The voidage of sand fluidized at 0.35 m/s in the presence of a shed is shown in Figure 9. The fluidized bed was rotated by 90°. The single-pulse images in Figure 9a are chaotic and show that the flow around the baffle is highly disturbed giving erratic local changes in voidage. In the averaged image, shown in Figure 9b, the area directly below the shed has considerably fewer particles (higher voidage) compared with the rest of the column, indicating that air is trapped beneath the shed. As expected, these images indicate that the shed has a significant effect on the dynamics of the flow.

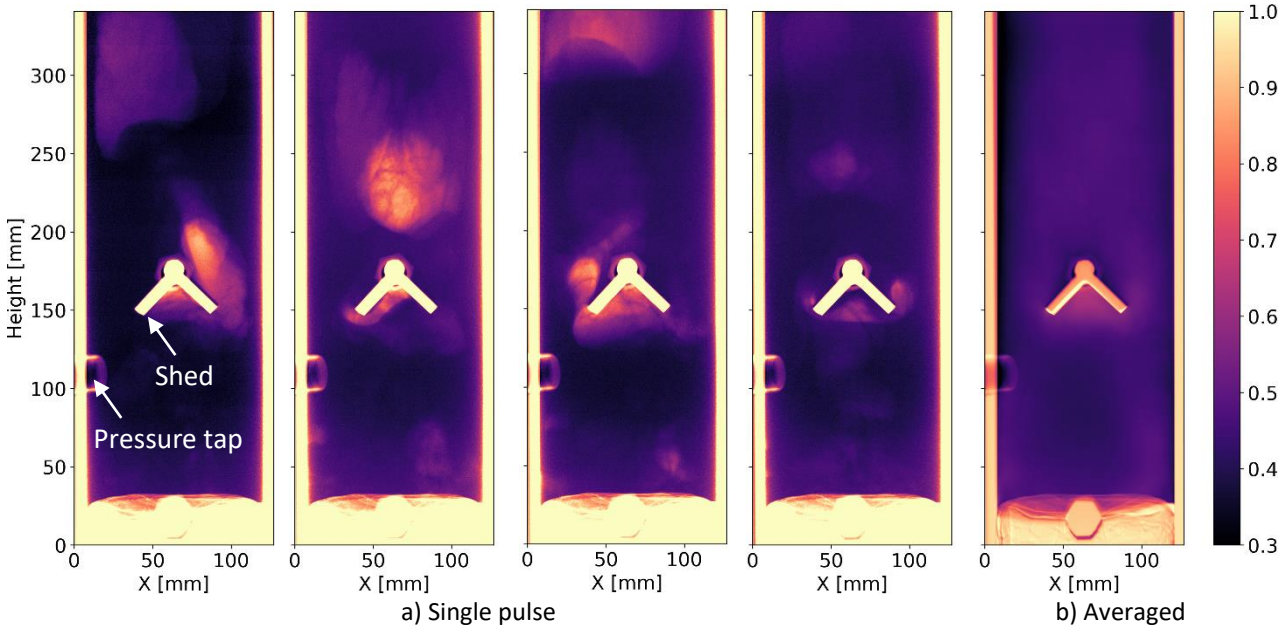

Figure 9 Voidage of fluidized sand particles at fluidization velocity u = 0.35 m/s with presence of a shed. The averaged image is effectively measured over 125 pulses. The slumped bed height of the column is 290 cm. The colormap shows the voidage value.

Cylindrical probes are commonly inserted into fluidized beds to characterize the bed behaviour. Often, the probe itself takes up a significant portion of the column cross-sectional area, and so is expected to alter the flow and performance of the fluidized bed under investigation. As shown in Figure 10, single-pulse and averaged multi-pulse voidage maps of sand, fluidized at a velocity 0.35 m/s are measured with the presence of an 18 mm cylindrical obstacle. In this case, the cylindrical obstacle is inserted to the depth equal to the diameter of the column. Figure 11 shows the result of the measurement for another experiment under the identical condition where the obstacle is only inserted to the center of the fluidized column.

The single-pulse images show no significant changes in voidage associated with the probe. The variation in voidage within these single-pulse images is due to the presence of fast-moving bubbles associated with the slugging regime. In Figure 10, both in the single-pulse and averaged multi-pulse images, directly underneath the probe tip there are slightly fewer particles (higher voidage), indicating that the probe marginally interrupts the adjacent flow. This behaviour is only visible when integrated along the entirety of the probe's length in Figure 10, implying that this disturbance to the flow is small. The apparent increase in particle number directly above the probe (lower voidage) in Figure 10 is an artifact from a metal fitting that mounts the probe. In all these images, and most clearly in the averaged multi-pulse image, the dynamics of the fluidized bed appear largely unaffected by the probe's presence. These results are encouraging in that they show an intrusive probe has a negligible effect on the bed hydrodynamics in the range of conditions studied here.

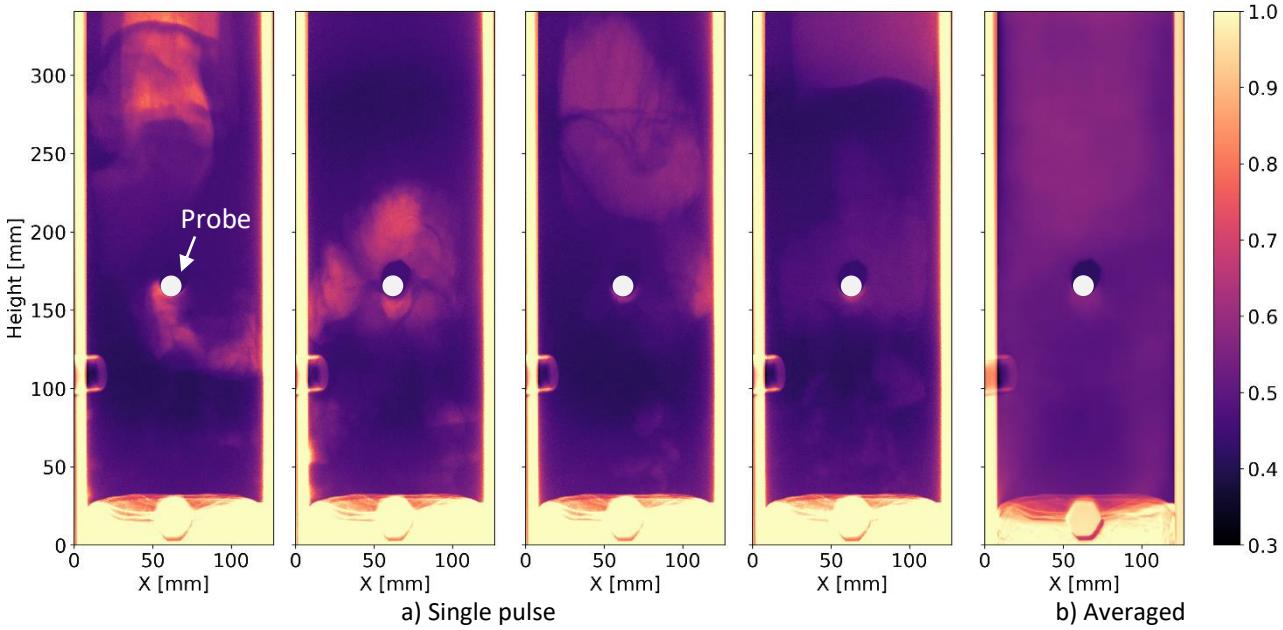

Figure 10 Voidage of fluidized sand particles at fluidization velocity u = 0.35 m/s with presence of a cylindrical obstacle. The averaged image is effectively measured over 125 pulses. The height of the cylinder is equal to the diameter of the column. The probe position is coloured in gray for clarity. The slumped bed height of the column is 290 cm. The colormap shows the voidage value.

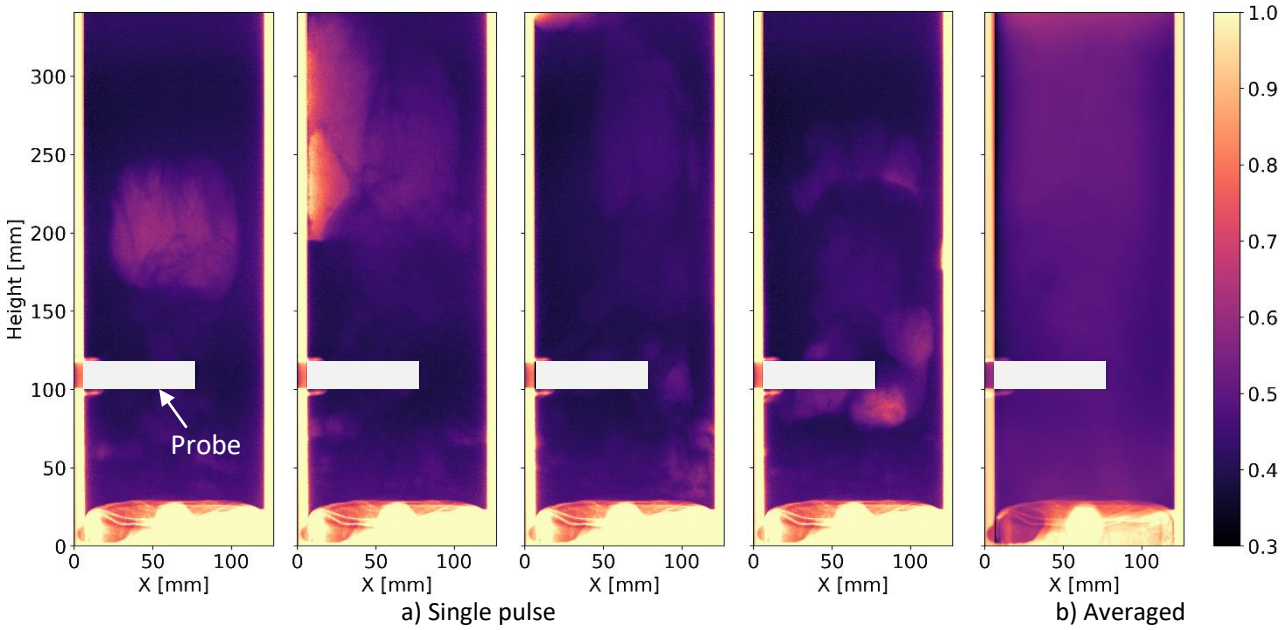

Figure 11 Voidage of fluidized sand particles at fluidization velocity u = 0.35 m/s with presence of a short cylindrical obstacle. The averaged image is effectively measured over 125 pulses. The height of the cylinder is equal to the diameter of the column. The probe position is coloured in gray for clarity. The slumped bed height of the column is 290 cm. The colormap shows the voidage value.

IV. Conclusions

Using a fast X-ray imaging system, we were able to produce voidage maps showing the instantaneous and time-averaged behaviour of two different fluidized solids in a 13 cm column. This diagnostic can non-intrusively probe the movement of solids within the bed, or other applications, informing on the internal dynamics of industrial processes. By benchmarking our system against two particle types (sand and FCC) at a variety of velocities covering several fluidization regimes, we were able to confirm that our X-ray and fluidized bed systems were behaving as expected, giving us the confidence to use these systems in more challenging environments. We used this knowledge to investigate the effect of bed internals on the fluidized hydrodynamics, specifically on the instantaneous and time-averaged voidage profiles. The first internal, a shed, was observed to disrupt the flow, trapping air beneath its tent-like shape. The second internal, a cylinder, was designed to mimic a measurement probe and was observed to minimally alter the flow adjacent to the obstacle and to leave the global flow unaltered. Both of these findings are the desired outcomes for each internal design and were easily demonstrated using this X-ray imaging system.

References

[1] F. Schillinger, T. J. Schildhauer, S. Maurer, E. Wagner, R. F. Mudde, and J. R. van Ommen, "Generation and evaluation of an artificial optical signal based on X-ray measurements for bubble characterization in fluidized beds with vertical internals," *Int. J. Multiph. Flow*, vol. 107, pp. 16–32, Oct. 2018, doi: 10.1016/j.ijmultiphaseflow.2018.03.002.

[2] J. Sun and Y. Yan, "Non-intrusive measurement and hydrodynamics characterization of gas–solid fluidized beds: a review," *Meas. Sci. Technol.*, vol. 27, no. 11, p. 112001, Sep. 2016, doi: 10.1088/0957-0233/27/11/112001.

[3] M. Rüdisüli, T. J. Schildhauer, S. M. A. Biollaz, and J. Ruud van Ommen, "Bubble characterization in a fluidized bed by means of optical probes," *Int. J. Multiph. Flow*, vol. 41, pp. 56–67, May 2012, doi: 10.1016/j.ijmultiphaseflow.2012.01.001.

[4] A. Acosta-Iborra, C. Sobrino, F. Hernández-Jiménez, and M. de Vega, "Experimental and computational study on the bubble behavior in a 3-D fluidized bed," *Chem. Eng. Sci.*, vol. 66, no. 15, pp. 3499–3512, Aug. 2011, doi: 10.1016/j.ces.2011.04.009.

[5] L. R. Glicksman, W. K. Lord, and M. Sakagami, "Bubble properties in large-particle fluidized beds," *Chem. Eng. Sci.*, vol. 42, no. 3, pp. 479–491, Jan. 1987, doi: 10.1016/0009-2509(87)80010-6.

[6] A. B. Whitehead, D. C. Dent, and G. N. Bhat, "Fluidisation studies in large gas-solid systems Part I: Bubble rise rates," *Powder Technol.*, vol. 1, no. 3, pp. 143–148, Oct. 1967, doi: 10.1016/0032-5910(67)80025-1.

[7] E. A. Whitemarsh, D. R. Escudero, and T. J. Heindel, "Probe effects on the local gas holdup conditions in a fluidized bed," *Powder Technol.*, vol. 294, pp. 191–201, Jun. 2016, doi: 10.1016/j.powtec.2016.02.035.

[8] S. Tebianian *et al.*, "Comparison of particle velocity measurement techniques in a fluidized bed operating in the square-nosed slugging flow regime," *Powder Technol.*, vol. 296, pp. 45–52, Aug. 2016, doi: 10.1016/j.powtec.2015.08.040.

[9] S. Maurer, E. Wagner, T. Schildhauer, J. R. Van Ommen, S. Biollaz, and R. F. Mudde, "X-ray measurements on the influence of optical probes on gas-solid fluidized beds," *Int. J. Multiph. Flow*, vol. 74, Apr. 2015, doi: 10.1016/j.ijmultiphaseflow.2015.04.002.

[10] S. Tebianian, N. Ellis, P. Lettieri, and J. R. Grace, "X-ray imaging for flow characterization and investigation of invasive probe interference in travelling fluidized bed," *Chem. Eng. Res. Des.*, vol. 104, pp. 191–202, Dec. 2015, doi: 10.1016/j.cherd.2015.08.006.

[11] W. Bai, N. G. Deen, and J. a. M. Kuipers, “Bubble properties of heterogeneous bubbly flows in a square bubble column,” *AIP Conf. Proc.*, vol. 1207, no. 1, pp. 563–568, Mar. 2010, doi: 10.1063/1.3366427.
[12] R. Xu, *Particle Characterization: Light Scattering Methods*. Springer Netherlands, 2002. Accessed: Sep. 22, 2019. [Online]. Available: https://www.springer.com/gp/book/9780792363002
[13] D. L. George, K. A. Shollenberger, J. R. Torczynski, T. J. O’Hern, and S. L. Ceccio, “Three-phase material distribution measurements in a vertical flow using gamma-densitometry tomography and electrical-impedance tomography,” *Int. J. Multiph. Flow*, vol. 27, no. 11, pp. 1903–1930, Nov. 2001, doi: 10.1016/S0301-9322(01)00042-8.
[14] F. T. Kühn, J. C. Schouten, R. F. Mudde, C. M. van den Bleek, and B. Scarlett, “Analysis of chaos in fluidization using electrical capacitance tomography,” *Meas. Sci. Technol.*, vol. 7, no. 3, pp. 361–368, Mar. 1996, doi: 10.1088/0957-0233/7/3/017.
[15] J. S. Halow, G. E. Fasching, P. Nicoletti, and J. L. Spenik, “Observations of a fluidized bed using capacitance imaging,” *Chem. Eng. Sci.*, vol. 48, no. 4, pp. 643–659, Feb. 1993, doi: 10.1016/0009-2509(93)80133-B.
[16] C. G. Xie, A. L. Stott, A. Plaskowski, and M. S. Beck, “Design of capacitance electrodes for concentration measurement of two-phase flow,” *Meas. Sci. Technol.*, vol. 1, no. 1, pp. 65–78, Jan. 1990, doi: 10.1088/0957-0233/1/1/012.
[17] R. K. Upadhyay and S. Roy, “Investigation of hydrodynamics of binary fluidized beds via radioactive particle tracking and dual-source densitometry,” *Can. J. Chem. Eng.*, vol. 88, no. 4, pp. 601–610, 2010, doi: 10.1002/cjce.20334.
[18] E. W. Grohse, “Analysis of gas-fluidized solid systems by x-ray absorption,” *AIChE J.*, vol. 1, no. 3, pp. 358–365, 1955, doi: 10.1002/aic.690010315.
[19] J. B. Romero and D. W. Smith, “Flash x-ray analysis of fluidized beds,” *AIChE J.*, vol. 11, no. 4, pp. 595–600, 1965, doi: 10.1002/aic.690110408.
[20] P. N. Rowe and B. A. Partridge, “An x-ray study of bubbles in fluidised beds,” *Chem. Eng. Res. Des.*, vol. 75, pp. S116–S134, Dec. 1965, doi: 10.1016/S0263-8762(97)80009-3.
[21] S. J. R. Simons, “Imaging techniques for fluidized bed systems: a review,” *Chem. Eng. J. Biochem. Eng. J.*, vol. 56, no. 3, pp. 83–93, Feb. 1995, doi: 10.1016/0923-0467(94)02902-4.
[22] R. F. Mudde, W. K. Harteveld, H. E. A. van den Akker, T. H. J. J. van der Hagen, and H. van Dam, “Gamma radiation densitometry for studying the dynamics of fluidized beds,” *Chem. Eng. Sci.*, vol. 54, no. 13, pp. 2047–2054, Jul. 1999, doi: 10.1016/S0009-2509(98)00372-8.
[23] A. Miller and D. Gidaspow, “Dense, vertical gas-solid flow in a pipe,” *AIChE J.*, vol. 38, no. 11, pp. 1801–1815, 1992, doi: 10.1002/aic.690381111.
[24] A. Toukan, V. Alexander, H. AlBazzaz, and M. H. Al-Dahhan, “Identification of flow regime in a cocurrent gas – Liquid upflow moving packed bed reactor using gamma ray densitometry,” *Chem. Eng. Sci.*, vol. 168, pp. 380–390, Aug. 2017, doi: 10.1016/j.ces.2017.04.028.
[25] J. Ma *et al.*, “Fluidization dynamics of cohesive Geldart B particles. Part I: X-ray tomography analysis,” *Chem. Eng. J.*, vol. 359, pp. 1024–1034, Mar. 2019, doi: 10.1016/j.cej.2018.11.082.
[26] D. Gidaspow and M. Driscoll, “Porosity and Pressure Waves in a Fluidized Bed of FCC Particles,” *Ind. Eng. Chem. Res.*, vol. 48, no. 5, pp. 2422–2429, Mar. 2009, doi: 10.1021/ie0716262.
[27] J. R. Van Ommen and R. F. Mudde, “Measuring the gas-solids distribution in fluidized beds - a review,” *Int. J. Chem. React. Eng. 612008*, 2008, doi: 10.2202/1542-6580.1796.
[28] F. Schillinger, “Systematic assessment and application of local optical and two-dimensional X-ray measurement techniques for hydrodynamic characterization of bubbling fluidized beds,” Doctoral Thesis, ETH Zurich, 2018. doi: 10.3929/ethz-b-000306127.

[29] R. F. Mudde, P. R. P. Bruneau, and T. H. J. J. van der Hagen, “Time-Resolved γ-Densitometry Imaging within Fluidized Beds,” *Ind. Eng. Chem. Res.*, vol. 44, no. 16, pp. 6181–6187, Aug. 2005, doi: 10.1021/ie049091p.
[30] D. R. Kaushal and Y. Tomita, “Experimental investigation for near-wall lift of coarser particles in slurry pipeline using γ-ray densitometer,” *Powder Technol.*, vol. 172, no. 3, pp. 177–187, Mar. 2007, doi: 10.1016/j.powtec.2006.11.020.
[31] M. Liu, Y. Zhang, H. Bi, J. R. Grace, and Y. Zhu, “Non-intrusive determination of bubble size in a gas–solid fluidized bed: An evaluation,” *Chem. Eng. Sci.*, vol. 65, no. 11, pp. 3485–3493, Jun. 2010, doi: 10.1016/j.ces.2010.02.049.
[32] M. Deza, N. P. Franka, T. J. Heindel, and F. Battaglia, “CFD Modeling and X-Ray Imaging of Biomass in a Fluidized Bed,” *J. Fluids Eng.*, vol. 131, no. 11, Oct. 2009, doi: 10.1115/1.4000257.
[33] R. F. Mudde, “Time-resolved X-ray tomography of a fluidized bed,” *Powder Technol.*, vol. 199, no. 1, pp. 55–59, Apr. 2010, doi: 10.1016/j.powtec.2009.04.021.
[34] R. F. Mudde, “Bubbles in a fluidized bed: A fast X-ray scanner,” *AIChE J.*, vol. 57, no. 10, pp. 2684–2690, 2011, doi: 10.1002/aic.12469.
[35] X. Chen, W. Zhong, and T. J. Heindel, “Orientation of cylindrical particles in a fluidized bed based on stereo X-ray particle tracking velocimetry (XPTV),” *Chem. Eng. Sci.*, vol. 203, pp. 104–112, Aug. 2019, doi: 10.1016/j.ces.2019.03.067.
[36] J. R. Grace, T. M. Knowlton, and A. A. Avidan, *Circulating Fluidized Beds*. Springer Science & Business Media, 2012.
[37] F. J. Sanchez Careaga, C. Briens, F. Berruti, J. McMillan, and M. Gray, “Agglomerate behavior in a recirculating fluidized bed with sheds: Effect of agglomerate properties,” *Powder Technol.*, vol. 275, pp. 263–272, May 2015, doi: 10.1016/j.powtec.2015.01.034.

Appendix

A. X-Ray Traverse

The X-ray traverse system is shown in Figure 12. The source and detector panel are both mounted to a common slewing (swivel) frame. Both the source and the detector panel can be independently moved radially and vertically on this frame. They are fixed to move axially together (slewing rotation). The frame includes integral measuring marks so that the operator can record the exact positions of the source and detector.

The source can traverse radially over approximately 53 cm from the center axis and can traverse vertically over approximately 66 cm. The detector can travel radially from approximately 38 cm to 91 cm from the center axis and can travel a vertical range of 71 cm. The entire slewing frame can rotate from 0° to 360°.

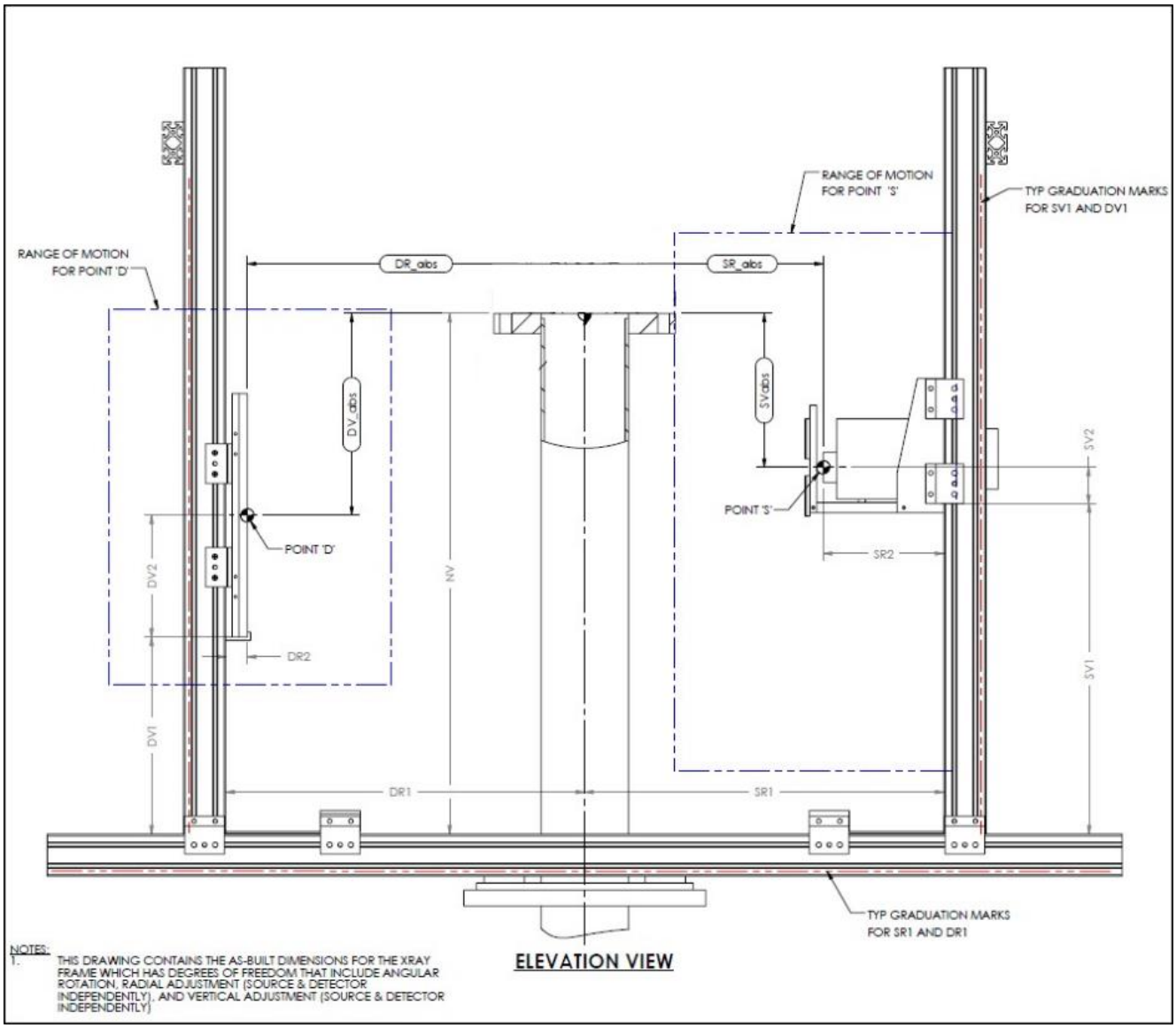

Figure 12 X-ray system drawing and traverse geometry.

B. X-ray Source Properties

This source does not produce X-rays using high-voltage tanks and a controlled current; instead, a high-voltage transient is produced across the X-ray tube from a spark jumping internally at a specified voltage. This technology enables ultra-fast exposure times for each pulse, allowing clear process images with no motion blur to be readily obtained. However, this technology does not allow either the X-ray current or voltage to be altered, there can be significant variation between pulses. To mitigate this variation, we apply a strict procedure using a well-described calibration staircase for every single shot.

The nominal specifications of our X-ray source are:

- 50 ns pulse time;
- 150 kVp X-ray tube potential;
- 2.6 mR/pulse dose rate (we observed about half this rate; converted to SI units the nominal rate is 2.1 µSv/pulse at 1 m but we recorded 1 - 1.3 µSv/pulse at 1 m with our survey meter);
- 10 pulses per second max pulse rate;
- 3 mm spot size;
- 200 pulses / 4 minutes max duty cycle.

C. Experimental fluidization regimes

Table 1 shows a summary of the fluidized bed parameters as mentioned in reference [36].

Table 1 Relevant parameters for characterizing air fluidized beds of sand and FCC. Here, g=9.81 m/s2 is the gravitational acceleration, D=0.12 m is the column diameter, μ_g=1.81 × 10-5 kg/(ms) is the gas viscosity, ρ_g=1.225 kg/m3 is the gas density.

Parameter	Sand	FCC	Formula [36]
Particle diameter, $\boldsymbol{d_p}$ [µm]	300	85	-
Bulk density, $\boldsymbol{\rho}$ [kg/m^3]	1600	940	-
Archimedes Number, Ar	1580	21.1	$g\, {d_p}^3 \rho_g \frac{\rho - \rho_g}{{\mu_g}^2}$
Minimum fluidization velocity, $\boldsymbol{U_{mf}}$ [m/s]	0.057	0.003	$\frac{\mu_g}{\rho_g d_p}\left(\sqrt{27.2^2 + 0.0408\, Ar} - 27.2\right)$
Minimum bubbling velocity, $\boldsymbol{U_{mb}}$ [m/s]	0.030*	0.008	$33\, d_p \left(\frac{\rho_g}{\mu_g}\right)^{0.1}$
Minimum slugging velocity, $\boldsymbol{U_{ms}}$ [m/s]	0.133	0.079	$U_{mf} + 0.07\sqrt{gD}$
Minimum turbulent velocity, $\boldsymbol{U_C}$ [m/s]	1.68	0.851	$\frac{\mu_g}{\rho_g d_p} 1.24\, Ar^{0.45}$ $(2 < Ar < 10^8)$
Minimum fast fluidization velocity, $\boldsymbol{U_{se}}$ [m/s]	3.00	1.223	$\frac{\mu_g}{\rho_g d_p} 1.53\, Ar^{0.5}$ $(2 < Ar < 4 \times 10^6)$

*Note that because for sand $U_{mb} < U_{mf}$ the minimum bubbling velocity is equivalent to the minimum fluidization velocity.